

3D tomographic velocity model estimation with CRS attributes

Eric Duveneck

email: eric.duveneck@mpi.uni-karlsruhe.de

keywords: tomography, attributes, velocity model

ABSTRACT

The 3D common-reflection-surface stack can be used to extract traveltimes information for inversion applications from seismic prestack data. A tomographic inversion method is presented that makes use of this information, in the form of first and second spatial derivatives of traveltimes—also called CRS attributes—to determine smooth, laterally inhomogeneous 3D subsurface velocity models for depth imaging.

The method is an extension of a recently presented 2D tomographic inversion based on CRS attributes. The input for the 3D inversion consists of picked CRS attributes at a number of locations in the simulated zero-offset volume obtained with the CRS stack. Compared to conventional reflection tomography, picking is considerably simplified, as only very few picks are required and these do not need to follow continuous horizons in the seismic data.

During the iterative inversion process, the required forward-modeled quantities are obtained by dynamic ray tracing along normal rays pertaining to the input data points. Fréchet derivatives for the tomographic matrix are calculated with ray perturbation theory. The inversion algorithm is demonstrated on a first synthetic data example, where the input data have directly been obtained by forward modeling.

INTRODUCTION

The construction of velocity models is an important task for seismic depth imaging in laterally inhomogeneous media. A number of different approaches for velocity model estimation have been proposed in the past, which differ in the criterion used to evaluate the model quality, in the determination of model updates, and in the parametrization of the model.

Migration velocity analysis methods are usually based on residual moveout analysis in common-image gathers (e.g., Al-Yahya, 1989; Deregowski, 1990). They require the repeated application of prestack migration and are, therefore, computationally very expensive.

Another frequently used technique for the determination of velocity models is reflection tomography (e.g., Farra and Madariaga, 1988; Stork and Clayton, 1991), in which the misfit between picked and modeled traveltimes is minimized by iteratively computing global model updates. Reflection tomography is often also combined with prestack migration (e.g., Stork, 1992). The drawback of tomographic methods, however, is the large amount of picking that is necessary to obtain traveltimes from the prestack data, usually along continuous reflectors across the entire seismic section. This picking becomes especially difficult, if not impossible, if the signal-to-noise (S/N) ratio in the data is low.

In a method introduced by Billette and Lambaré (1998) and Billette et al. (2003), called stereotomography, slope information of locally coherent events is used together with traveltimes to obtain a smooth velocity model. With that approach, no interfaces have to be introduced in the model, and only locally coherent events need to be considered during picking.

Recently, a tomographic method for the construction of smooth velocity models based on the results of the common-reflection-surface (CRS) stack has been presented by Duveneck and Hubral (2002) and Du-

veneck (2004). This approach, which combines aspects of stacking-velocity based inversion methods with concepts related to stereotomography, makes use of kinematic information in the form of wavefront curvatures and emergence angles extracted from the prestack data by means of the CRS stack. The method is especially well suited for an application to data, in which reflection events cannot be identified continuously in the prestack data. Picking is considerably simplified by the fact that it is performed in a stacked section of high S/N ratio. Compared to conventional reflection tomography, only very few picks are required and these do not need to follow events continuously across the section.

In this paper, I will present a reformulation and extension of this CRS-stack-based method to the 3D case. Instead of wavefront curvatures and emergence angles, the 3D version of the method is formulated in terms of first and second spatial traveltime derivatives, which are equivalent to emergence angle and wavefront curvature information, but do not require the specification of a constant near-surface velocity value.

In the following, the 3D CRS operator and the associated kinematic wavefield attributes will be briefly explained. These attributes will then be used to formulate the tomographic inversion method. It is based on the criterion that in the correct model, so-called normal-incidence-point (NIP) waves that can be associated with the kinematic wavefield attributes should focus at zero traveltime in the subsurface. Finally, a first test of the algorithm on synthetic data will be presented and aspects related to the application to real seismic data will be discussed.

3D CRS STACK AND ATTRIBUTES

The CRS stack (e. g., Jäger et al., 2001) has originally been developed to obtain simulated zero-offset (ZO) sections or volumes from seismic multicoverage data. The method is based on stacking operators that are of second order in the half-offset \mathbf{h} and midpoint $\boldsymbol{\xi}$ coordinates defined in the general 3D case by

$$\mathbf{h} = (\mathbf{x}_g - \mathbf{x}_s) / 2 \quad \text{and} \quad \boldsymbol{\xi} = (\mathbf{x}_g + \mathbf{x}_s) / 2, \quad (1)$$

where \mathbf{x}_s and \mathbf{x}_g are two-component vectors containing the source and receiver coordinates, respectively.

The shape of the CRS stacking operator at a given zero-offset location $(\boldsymbol{\xi}_0, t_0)$ is determined by a number of parameters related to the coefficients of the traveltime expansion. For each zero-offset sample to be simulated, the optimum stacking operator is found by varying the parameter values, i.e., the shape of the operator, and performing a coherence analysis directly in the prestack data. The parameters, which yield the highest coherence value and, thus, describe the optimum stacking operator, are called kinematic wavefield attributes.

If a locally constant near-surface velocity v_0 is assumed to be known, the CRS operator may be written in a form that allows the interpretation of the kinematic wavefield attributes as parameters describing two hypothetical emerging wavefronts at the considered surface location $\boldsymbol{\xi}_0$: These are the so-called normal-incidence point (NIP) wave and the normal (N) wave (e. g., Hubral, 1983). The NIP wave would be observed at $\boldsymbol{\xi}_0$ if a point-source were placed at the NIP of the zero-offset ray on a reflector in the subsurface, while an N wave would be obtained if an exploding reflector element were placed at the NIP in the subsurface.

In the 3D case, the emerging wavefronts are locally characterized by their curvatures and their emergence direction at $\boldsymbol{\xi}_0$, which is the same for the NIP and the N wave. If the NIP wave and N wave curvatures are given by 2×2 curvature matrices $\underline{\mathbf{K}}_{\text{NIP}}$ and $\underline{\mathbf{K}}_{\text{N}}$, respectively (each matrix contains three independent elements), and the emergence direction is described by two angles α and ψ (emergence angle and azimuth), the 3D CRS operator reads (e. g., Höcht, 2002)

$$t^2(\Delta\boldsymbol{\xi}, \mathbf{h}) = (t_0 + 2 \mathbf{p}_\xi \cdot \Delta\boldsymbol{\xi})^2 + 2t_0 (\Delta\boldsymbol{\xi}^T \underline{\mathbf{M}}_\xi \Delta\boldsymbol{\xi} + \mathbf{h}^T \underline{\mathbf{M}}_h \mathbf{h}) \quad (2)$$

with

$$\begin{aligned} \mathbf{p}_\xi &= \frac{1}{2} \partial t / \partial \boldsymbol{\xi} = \frac{1}{v_0} (\sin \alpha \cos \psi, \sin \alpha \sin \psi)^T \\ \underline{\mathbf{M}}_h &= \frac{1}{2} \partial^2 t / \partial \mathbf{h}^2 = \frac{1}{v_0} \underline{\mathbf{H}} \underline{\mathbf{K}}_{\text{NIP}} \underline{\mathbf{H}}^T \\ \underline{\mathbf{M}}_\xi &= \frac{1}{2} \partial^2 t / \partial \boldsymbol{\xi}^2 = \frac{1}{v_0} \underline{\mathbf{H}} \underline{\mathbf{K}}_{\text{N}} \underline{\mathbf{H}}^T \end{aligned} \quad (3)$$

Here, the matrix $\underline{\mathbf{H}}$ is the 2×2 upper left sub-matrix of the transformation matrix from the local ray-centered Cartesian coordinate system to the Cartesian coordinate system associated with the measurement surface (e. g., Červený, 2001), t_0 is the two-way traveltimes along the zero-offset ray, and $\Delta\xi = \xi - \xi_0$. The matrix $\underline{\mathbf{H}}$ also depends on the angles α and ψ . A similar expression has been derived by Ursin (1982).

Alternatively to the wavefront curvatures and emergence angles given above, the vector \mathbf{p}_ξ and the matrices $\underline{\mathbf{M}}_h$ and $\underline{\mathbf{M}}_\xi$ themselves or, more precisely, their components may be regarded as kinematic wavefield attributes. As indicated in equation (3), these describe the first and second derivatives of the reflection traveltime surface with respect to the offset and midpoint coordinates and are, thus, directly related to the Taylor coefficients of the second order expansion of t around $\mathbf{h} = \mathbf{0}$ and $\xi = \xi_0$ (e. g., Schleicher et al., 1993). Due to reciprocity, i.e., the invariance of traveltimes with respect to interchanging source and receiver locations, the traveltime surface is symmetrical around $\mathbf{h} = \mathbf{0}$. Therefore, the first derivative of t with respect to the offset is zero.

The reflection traveltimes measured in a common-midpoint (CMP) gather do not, in general, strictly correspond to a common-reflection point in the subsurface. It has, however, been shown, e.g., by Hubral and Krey (1980), that these traveltimes coincide up to second order in \mathbf{h} with those that would be obtained if all involved rays passed through the NIP of the zero-offset ray (NIP wave theorem). The corresponding ray branches would then be the same as those associated with the NIP wave. This justifies the relation of the matrix $\underline{\mathbf{M}}_h$, obtained from observations in the CMP gather, to the NIP wave curvature $\underline{\mathbf{K}}_{\text{NIP}}$, equation (3). In fact, $\underline{\mathbf{M}}_h$ is the matrix of second derivatives of traveltime with respect to the receiver location that would be obtained at the location ξ_0 due to an emerging NIP wave. It is related to the azimuth-dependent NMO velocity v_{NMO} by

$$\frac{1}{v_{\text{NMO}}^2(\phi)} = 2 t_0 \hat{\mathbf{e}}_\phi \underline{\mathbf{M}}_h \hat{\mathbf{e}}_\phi^T, \quad (4)$$

where the unit vector $\hat{\mathbf{e}}_\phi = (\cos \phi, \sin \phi)$ defines the azimuth direction (e. g. Hubral and Krey, 1980; Gjøystdal et al., 1984).

During the 3D CRS stack, along with the simulated ZO volume a number of volumes containing the optimum kinematic wavefield attributes for each ZO sample are obtained. In addition, the CRS stack yields a coherence (e. g., semblance) section, that carries information on how well the CRS operator could be fitted to reflection events in the data. Where no reflection events have been detected, the coherence will be low and the corresponding obtained kinematic wavefield attributes will not be reliable. If the acquisition geometry is restricted to certain azimuth ranges, as, e. g., in marine acquisition, the second derivative of traveltime in the CMP gather may only be determined in this azimuth direction. Instead of the matrix $\underline{\mathbf{M}}_h$, only the component

$$M_\phi = \hat{\mathbf{e}}_\phi \underline{\mathbf{M}}_h \hat{\mathbf{e}}_\phi^T \quad (5)$$

associated with the azimuth direction ϕ may then be extracted from the prestack data.

3D TOMOGRAPHY WITH KINEMATIC WAVEFIELD ATTRIBUTES

As shown in the previous section, the parameters describing the approximate traveltime field of an emerging NIP wave at the location ξ_0 can be extracted from the prestack data, e. g., with the CRS stack. Alternatively, a conventional velocity analysis and an additional local dip search in the stacked volume may be used.

It has been recognized by a number of authors that these NIP wave parameters (either in terms of traveltime derivatives or in terms of wavefront curvatures and emergence angles) contain information that allows to deduce the laterally inhomogeneous subsurface distribution of seismic velocities (e. g., Chernyak and Gritsenko, 1979; Hubral and Krey, 1980).

Inversion algorithms can be based on the criterion that in a correct velocity model all considered NIP waves, when propagated back into the subsurface along the corresponding normal ray, should focus at zero traveltime at the NIP. Conventional algorithms based on this criterion proceed in a layer-stripping manner, assuming a velocity model consisting of layers separated by curved interfaces (e. g., Hubral and Krey, 1980; Biloti et al., 2002). This model parametrization restricts the applicability of the inversion to regions with a corresponding simple geology and to data, in which reflection events may be identified continuously throughout the entire section (or volume, respectively).

Duveneck (2004) presents an alternative 2D tomographic velocity model estimation approach based on NIP wave parameters, which overcomes the above-mentioned limitations. The method described there

uses a smooth velocity model description based on 2D B-splines and allows to drop the assumption of continuous curved reflectors, thus considerably broadening its applicability. In this paper, the tomographic approach of Duveneck (2004) will be extended to the 3D case.

Input data

For the formulation of a 3D tomographic inversion based on the focusing of NIP waves, the time-domain versions of the attributes, equation (3), will be used. An emerging NIP wave is, thus, characterized by the one-way traveltimes along the normal ray, $\tau = t_0/2$, the observed horizontal slowness \mathbf{p}_ξ at ξ_0 , and the observed second derivatives of (one-way) traveltimes, given by the matrix $\underline{\mathbf{M}}_h$.

Apart from computational benefits discussed below, the time-domain versions of the kinematic wave-field attributes have the advantage that they can be directly determined from the prestack data (e. g., with the CRS operator (2)), without having to assume a value for the near-surface velocity v_0 . If the entire matrix $\underline{\mathbf{M}}_h$ can be determined from the data, it can in principle be used for a tomographic inversion. If due to a limited acquisition geometry, only the component M_ϕ associated with a certain azimuth ϕ can be obtained, this information will also be sufficient for a tomographic inversion. Data points used as input for the tomography are, thus, given by

$$(\tau, M_\phi, p_{\xi_x}, p_{\xi_y}, \xi_x, \xi_y)_i \quad i = 1, \dots, n_{\text{data}}, \quad (6)$$

where the notations $\tau = t_0/2$, $\mathbf{p}_\xi = (p_{\xi_x}, p_{\xi_y})^T$, and $\xi_0 = (\xi_x, \xi_y)^T$ have been used. These data are extracted automatically from the CRS attribute volumes at pick locations (ξ_0, t_0) in the CRS stack volume. As noted above, the picks do not need to follow reflection events continuously across the entire ZO volume. Rather, each data point can be considered independently of the others and may lie on an event that is only locally coherent. The reliability of each data pick is determined by the associated CRS coherence value. In fact, picking may be automated based on the information contained in the CRS coherence volume.

Model parameters

The obvious way of implementing the inversion would be to propagate the NIP waves associated with the data points (6) into the subsurface in an initial velocity model and iteratively update the model until all considered NIP waves focus at zero traveltimes.

As discussed in Duveneck (2004), the inversion process becomes more stable if the modeling direction is reversed, i. e., the NIP wave propagation is started in the subsurface at the respective NIP location. In the optimum model sought during the inversion, the misfit between the forward-modeled NIP parameters and those given by the corresponding data points (6) is minimized. That way, possible errors and noise in all considered data components may be accounted for.

The true subsurface locations of the NIPs and the corresponding local reflector dips associated with the picked data points are initially unknown. Therefore, they have to be considered as additional model parameters to be determined during the inversion. In the 3D case, the NIPs corresponding to the data points given in (6) are characterized by the parameters

$$(x, y, z, e_x, e_y)_i \quad i = 1, \dots, n_{\text{data}}, \quad (7)$$

where e_x and e_y are the horizontal components of a three-component unit vector $\hat{\mathbf{e}}$ that defines the normal ray direction. i. e., the local reflector normal at the NIP.

The velocity model itself is, as in the 2D case described by Duveneck (2004), defined in terms of B-spline functions of degree four (e. g., de Boor, 1978). In three dimensions, the velocity model as a function of coordinates (x, y, z) is given by

$$v(x, y, z) = \sum_{j=1}^{n_x} \sum_{k=1}^{n_y} \sum_{l=1}^{n_z} v_{jkl} \beta_j(x) \beta_k(y) \beta_l(z), \quad (8)$$

where n_x , n_y , and n_z are the chosen numbers of B-spline knots, and $\beta_j(x)$, $\beta_k(y)$, and $\beta_l(z)$ are B-spline basis functions. The model parameters determining the distribution of seismic velocities in the model are,

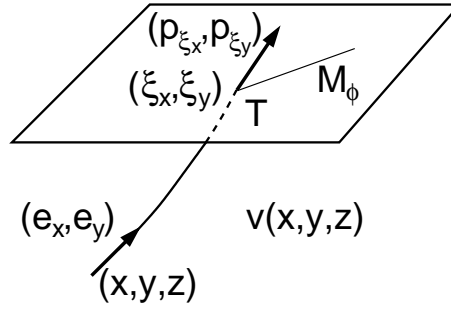


Figure 1: Definition of model and data components for the tomographic inversion. See text for details.

thus,

$$v_{jkl}, \quad j = 1, \dots, n_x, \quad k = 1, \dots, n_y, \quad l = 1, \dots, n_z. \quad (9)$$

The parameters (7) characterizing the NIP, together with the B-spline coefficients given in (9) constitute the model parameters to be determined during the tomographic inversion.

Forward modeling

In the course of the inversion process, forward modeling of the quantities (6) for given model parameters needs to be performed. This can be done in an efficient way by dynamic ray tracing. If a reduced ray-tracing system in Cartesian coordinates is used, where the z -coordinate is the independent parameter along the ray (see Appendix), the associated ray propagator matrix coincides with the surface-to-surface propagator matrix

$$\underline{\mathbf{T}} = \begin{pmatrix} \underline{\mathbf{A}} & \underline{\mathbf{B}} \\ \underline{\mathbf{C}} & \underline{\mathbf{D}} \end{pmatrix} \quad (10)$$

introduced by Bortfeld (1989) specialized to the case of horizontal anterior and posterior surfaces. (This in no way implies a limitation to horizontal reflectors, as only a point source response—the NIP wave—is modeled.) The matrix $\underline{\mathbf{M}}_h$ of second derivatives of NIP wave traveltime can then be calculated directly from the 2×2 submatrices of $\underline{\mathbf{T}}$ (e. g., Červený, 2001):

$$\underline{\mathbf{M}}_h = \underline{\mathbf{D}} \underline{\mathbf{B}}^{-1}. \quad (11)$$

The use of z as the independent parameter during ray tracing limits the applicability to rays which have no turning point with respect to z (which is no problem in practice), but has clear advantages in that the number of equations to be solved is reduced and complicated transformations to and from ray-centered coordinates are avoided. The traveltime along the normal ray and the horizontal components of the slowness vector at the location ξ_0 are directly obtained from kinematic ray tracing.

Solution of the inverse problem

The inverse problem to be solved can be formally stated as follows: we try to find a model vector \mathbf{m} , consisting of the elements given in (7) and (9), that minimizes the misfit between a data vector \mathbf{d} , containing the picked values given in (6), and the corresponding modeled values $\mathbf{d}_{\text{mod}} = \mathbf{f}(\mathbf{m})$. The operator \mathbf{f} symbolizes the dynamic ray tracing in the given model. As a measure of misfit the least-squares norm (e. g., Tarantola, 1987) is used. The modeling operator \mathbf{f} is nonlinear, therefore a solution to the inverse problem is found in an iterative way by locally linearizing \mathbf{f} and applying linear least-squares minimization during each iteration. In addition, a regularization term needs to be introduced to stabilize the inversion. This is realized by requiring the velocity model to be as smooth as possible, i. e., to have minimum second derivatives. A model update $\Delta \mathbf{m}$ is found by computing the least-squares solution of a matrix equation of the form

$$\hat{\underline{\mathbf{F}}} \Delta \mathbf{m} = \Delta \hat{\mathbf{d}}, \quad (12)$$

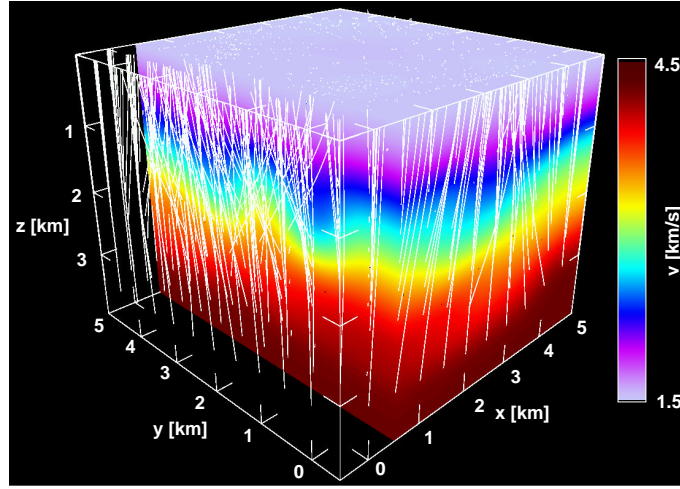


Figure 2: Smooth velocity model and normal ray trajectories. The velocity model is described by B-splines with $n_x \times n_y \times n_z = 9 \times 9 \times 9 = 729$ knot locations spaced 500 m horizontally and 400 m vertically. Data were modeled along 1008 normal rays.

where

$$\hat{\mathbf{F}} = \begin{pmatrix} \underline{\mathbf{C}}_D^{-\frac{1}{2}} \underline{\mathbf{F}} \\ \underline{\mathbf{0}}, \underline{\mathbf{B}} \end{pmatrix}, \quad \Delta \hat{\mathbf{d}} = \begin{pmatrix} \underline{\mathbf{C}}_D^{-\frac{1}{2}} \Delta \mathbf{d}(\mathbf{m}_n) \\ -\underline{\mathbf{0}}, \underline{\mathbf{B}} \mathbf{m}_n \end{pmatrix}. \quad (13)$$

Here, $\Delta \mathbf{d}(\mathbf{m}_n) = \mathbf{d} - \mathbf{f}(\mathbf{m}_n)$ is the data error after the n th iteration and $\underline{\mathbf{F}}$ is a matrix containing the Fréchet derivatives of \mathbf{f} at \mathbf{m}_n . These can be obtained during forward modeling by application of ray perturbation theory (Farra and Madariaga, 1987) along each considered ray. The corresponding expressions are given in Appendix A. The matrix $\underline{\mathbf{C}}_D$ in (13) is a diagonal matrix containing weights for the different data components, while the matrix $\underline{\mathbf{B}}$ is related to the matrix $\underline{\mathbf{D}}$ in the regularization term of the cost function: $\underline{\mathbf{B}}^T \underline{\mathbf{B}} = \epsilon \underline{\mathbf{D}}$. The cost function to be minimized by the solution of (12) is, thus, given by

$$S(\mathbf{m}) = \frac{1}{2} \Delta \mathbf{d}^T(\mathbf{m}) \underline{\mathbf{C}}_D^{-1} \Delta \mathbf{d}(\mathbf{m}) + \frac{1}{2} \epsilon \mathbf{m}_{(v)}^T \underline{\mathbf{D}} \mathbf{m}_{(v)}, \quad (14)$$

where $\mathbf{m}_{(v)}$ represents that part of the model vector, which contains the B-spline coefficients, and the factor ϵ weights the relative contribution of the regularization to the cost function. The matrix $\underline{\mathbf{D}}$ defines a measure of roughness of the velocity model in terms of the corresponding model parameters. Equation (12) is solved with the LSQR algorithm (Paige and Saunders, 1982a,b). Details of the solution strategy and regularization are discussed in Duvencek (2004).

SYNTHETIC DATA EXAMPLE

In order to test the inversion algorithm described in the previous section, it is applied to synthetic data that have directly been obtained by dynamic ray-tracing modeling in a smooth inhomogeneous velocity model defined by B-splines. In the presented example, see Figure 2, a total of $n_x \times n_y \times n_z = 9 \times 9 \times 9 = 729$ B-spline knot locations with a knot spacing of 500 m in the horizontal and 400 m in the vertical direction have been used. Three vertical cuts through the model are displayed in the left column of Figure 3.

The ray starting locations of the normal rays (i. e., the NIP locations) used to model the input data are, for the purposes of this synthetic test, distributed on iso-velocity surfaces in the model (every 400 m/s) and have a horizontal separation of 500 m in the x - and y -direction, see Figure 5, left. The initial slowness vector for each ray is oriented perpendicularly to the iso-velocity surfaces. Thus, the reflection points used for modeling follow the velocity structure, which is reasonable.

Selected components (i. e., the values for τ , M_ϕ , p_{ξ_x} , and ξ_x) of the obtained 1008 modeled data points are shown in the left column of Figure 4. They simulate the input data (6) that would be picked and

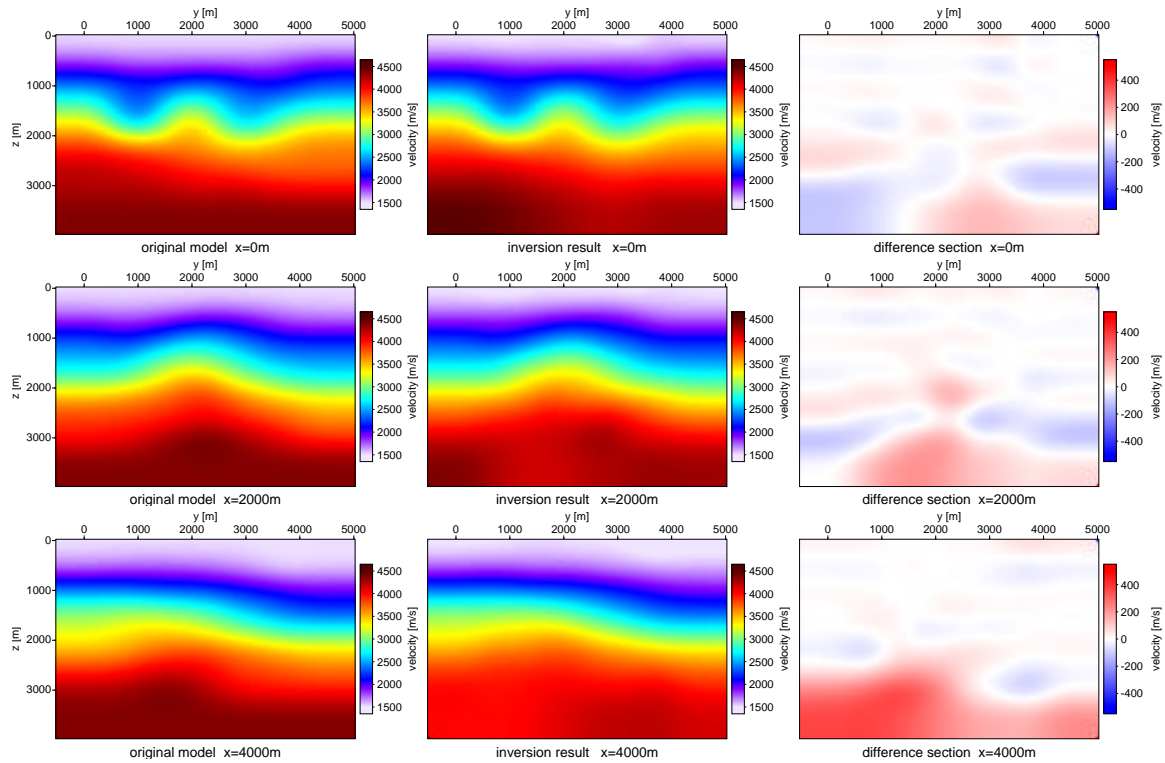


Figure 3: Crossline slices at $x=0$ m, $x=2000$ m, and $x=4000$ m through the original model (left), the reconstructed model (center), and the difference between original and reconstructed models (right).

extracted from the CRS stack results in a real data application. The values of M_ϕ correspond to an azimuth of $\phi = 0^\circ$ (i. e., the x -direction). These sparse data are used as input for the tomographic inversion in order to reconstruct the 3D smooth velocity model, Figure 2.

Vertical cuts through the inversion result obtained after 12 iterations are displayed in the central column of Figure 3. The right column of Figure 3 shows difference sections obtained by subtracting the reconstructed model from the true model. Differences are mainly visible in the lower part of the model, where ray-coverage is insufficient. Apart from these regions, the velocity model is well reconstructed, which is a notable result, considering the sparsity of the input data. As in the 2D case (Duveneck, 2004), the trajectories of the normal rays (not shown) are obtained as an inversion result along with the velocity model itself. Residual data errors of the data components τ , M_ϕ , p_{ξ_x} , and ξ_x are plotted in the right column of Figure 4, while the absolute residual depth error of the NIPs is displayed in Figure 5, right.

DISCUSSION

In the synthetic data example presented in the previous section, perfect input data without noise have been used. Results obtained with noisy input data derived from synthetic and real seismic data in the 2D case (Duveneck, 2004; Heilmann et al., 2004) suggest that noisy input data should be handled as well with the 3D algorithm presented here.

During the inversion, additional constraints on the velocity model may be introduced. If a priori velocity information at certain points in the subsurface is available (e. g., from boreholes or from near-surface measurements), this information may be included in the inversion. It is treated as additional data, with a corresponding data error that is minimized during the inversion. Another constraint on the velocity model may be that of requiring the velocity distribution to locally follow the reflector structure (at the NIP locations associated with the input data). This is implemented by adding an extra term to the cost function (14) to minimize first derivatives of the velocity distribution in the plane perpendicular to the normal ray

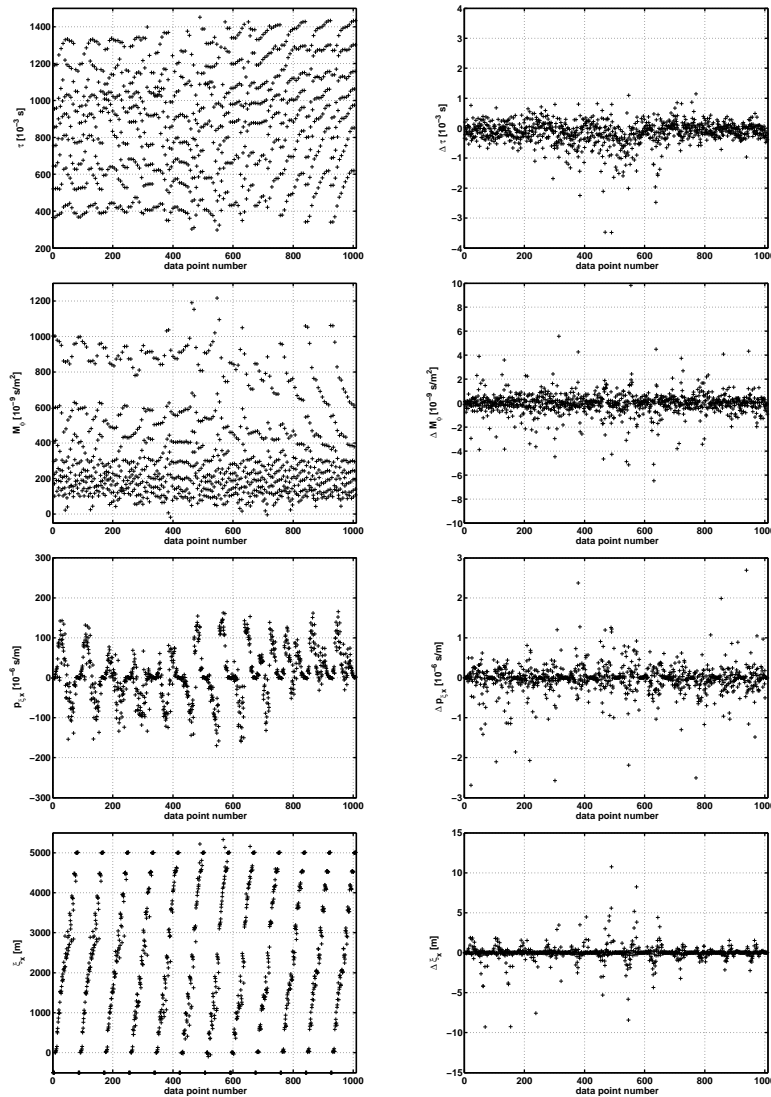


Figure 4: Data components τ , M_ϕ , p_{ξ_x} , ξ_x (left) and their residual errors after 12 iterations (right).

at all NIP locations during each iteration of the inversion. Such a constraint has proven to be useful in the application of the 2D tomographic inversion with kinematic wavefield attributes.

Another important point to be addressed is the picking of the input data. One of the advantages of the inversion method presented here is that, compared to conventional reflection tomography, very few picks are required. Each pick already represents the approximate multi-offset reflection traveltimes, represented by the kinematic wavefield attributes. Pick locations may be considered independently of each other and picking is performed in a stacked section (the CRS stack section). Still, picking in 3D data volumes can be tedious. However, as noted above, the CRS stack process provides information useful for automated picking in the form of the coherence volume. For 2D tomography with kinematic wavefield attributes, a simple automatic picking tool based on the CRS coherence section has been implemented and successfully applied to real data. Applied to seismic data with a reasonable S/N ratio, this approach should also work with 3D data. Multiple reflections should, however, be removed before an automated picking procedure is applied, as these are difficult to distinguish from primary reflection events. Alternatively, in simple situations, picks corresponding to multiples can be identified by abnormal values of M_ϕ and may be removed prior to the inversion. Due to the use of traveltimes approximations to describe the kinematics of reflection

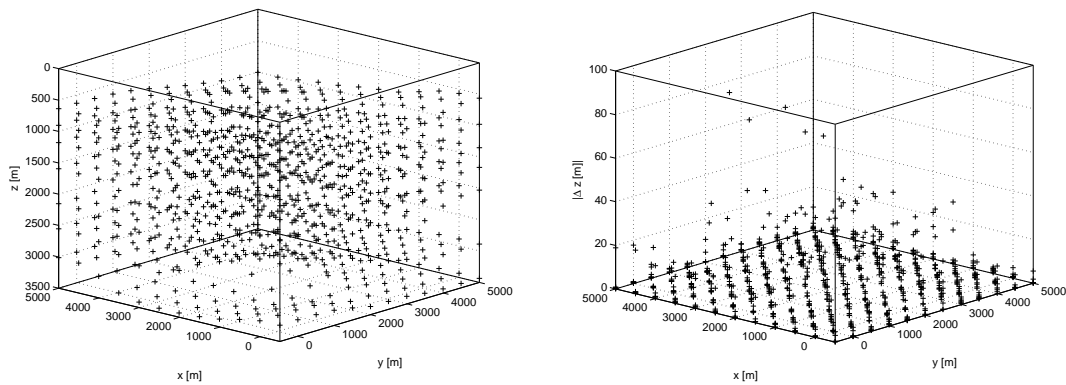


Figure 5: The 1008 subsurface points (NIPs) used to model the input data (left) and residual absolute depth errors after 12 iterations (right).

events, the subsurface velocity structure may be laterally inhomogeneous, but not arbitrarily complex.

CONCLUSIONS

In this paper, a 3D tomographic method for the determination of velocity models for depth imaging has been presented. The method uses kinematic wavefield attributes extracted from the prestack data with the 3D CRS stack. The required attributes consist of first and second spatial derivatives of traveltimes associated with hypothetical emerging NIP waves. The inversion is based on the well-known concept that in a correct model, all NIP waves should focus at zero traveltimes.

The 3D method presented here is an extension and modification of a previously published 2D tomographic inversion with kinematic wavefield attributes. The method should be particularly suitable for the application to seismic data with a relatively low S/N ratio, where identifying and picking of reflection events in the prestack data, as required for conventional reflection tomography, is difficult. Picking of the input data for the CRS-attribute-based tomography is performed in the stacked section, and only very few picks are required. Picking can, in principle be automated based on the coherence section obtained with the CRS stack. An initial test of the 3D tomographic inversion algorithm on a synthetic example shows the potential of the method. Further tests on 3D synthetic and real seismic data are, however, required.

ACKNOWLEDGMENTS

This work was kindly supported by the sponsors of the *Wave Inversion Technology (WIT) Consortium*, Karlsruhe, Germany.

REFERENCES

- Al-Yahya, K. (1989). Velocity analysis by iterative profile migration. *Geophysics*, 54(6):718–729.
- Billette, F. and Lambaré, G. (1998). Velocity macro-model estimation from seismic reflection data by stereotomography. *Geophys. J. Int.*, 135:671–690.
- Billette, F., Le Bégat, S., Podvin, P., and Lambaré, G. (2003). Practical aspects of 2D stereotomography. *Geophysics*, 68(3):1008–1021.
- Biloti, R., Santos, L. T., and Tygel, M. (2002). Multiparametric traveltimes inversion. *Stud. geophys. geod.*, 46:177–192.
- Bortfeld, R. (1989). Geometrical ray theory: Rays and traveltimes in seismic systems (second-order approximation of the traveltimes). *Geophysics*, 54(3):342–349.
- Červený, V. (2001). *Seismic Ray Theory*. Cambridge University Press.

- Chernyak, V. S. and Gritsenko, S. A. (1979). Interpretation of the effective common-depth-point parameters for a three-dimensional system of homogeneous layers with curvilinear boundaries. *Geologiya i Geofizika*, 20(12):112–120.
- de Boor, C. (1978). *A practical guide to splines*. Springer-Verlag.
- Deregowski, S. M. (1990). Common-offset migrations and velocity analysis. *First Break*, 8(6):224–234.
- Duveneck, E. (2004). Velocity model estimation with data-derived wavefront attributes. *Geophysics*, 69. In print.
- Duveneck, E. and Hubral, P. (2002). Tomographic velocity model inversion using kinematic wavefield attributes. In *72nd Ann. Internat. Mtg., Expanded Abstracts*, pages 862–865. Soc. Expl. Geophys.
- Farra, V. and Madariaga, R. (1987). Seismic waveform modeling in heterogeneous media by ray perturbation theory. *J. Geophys. Res.*, 92(B3):2697–2712.
- Farra, V. and Madariaga, R. (1988). Non-linear reflection tomography. *Geophys. J.*, 95:135–147.
- Gjøystdal, H., Reinhardsen, J. E., and Ursin, B. (1984). Traveltime and wavefront curvature calculations in three-dimensional inhomogeneous layered media with curved interfaces. *Geophysics*, 49(9):1466–1494.
- Heilmann, Z., Mann, J., Duveneck, E., and Hertweck, T. (2004). CRS-stack-based seismic imaging workflow—a real data example. *Wave-Inversion-Technology (WIT) Report 2003*.
- Höcht, G. (2002). *Traveltime approximations for 2D and 3D media and kinematic wavefield attributes*. PhD thesis, University of Karlsruhe.
- Hubral, P. (1983). Computing true amplitude reflections in a laterally inhomogeneous earth. *Geophysics*, 48(8):1051–1062.
- Hubral, P. and Krey, T. (1980). *Interval velocities from seismic reflection traveltime measurements*. Soc. Expl. Geophys.
- Jäger, R., Mann, J., Höcht, G., and Hubral, P. (2001). Common-reflection-surface stack: Image and attributes. *Geophysics*, 66(1):97–109.
- Paige, C. C. and Saunders, M. A. (1982a). Algorithm 583 – LSQR: Sparse linear equations and least squares problems. *ACM Trans. Math. Softw.*, 8(2):195–209.
- Paige, C. C. and Saunders, M. A. (1982b). LSQR: An algorithm for sparse linear equations and sparse least squares. *ACM Trans. Math. Softw.*, 8(1):43–71.
- Schleicher, J., Tygel, M., and Hubral, P. (1993). Parabolic and hyperbolic paraxial two-point traveltimes in 3D media. *Geophys. Prosp.*, 41:495–513.
- Stork, C. (1992). Reflection tomography in the postmigrated domain. *Geophysics*, 57(5):680–692.
- Stork, C. and Clayton, R. W. (1991). Linear aspects of tomographic velocity analysis. *Geophysics*, 56(4):483–495.
- Tarantola, A. (1987). *Inverse Problem Theory: Methods for Data Fitting and Model Parameter Estimation*. Elsevier, Amsterdam.
- Ursin, B. (1982). Quadratic wavefront and traveltime approximations in inhomogeneous layered media with curved interfaces. *Geophysics*, 47:1012–1021.

APPENDIX A

Ray tracing and Fréchet derivatives

The Fréchet derivatives $\partial(\tau, M_\phi, p_{\xi_x}, p_{\xi_y}, \xi_x, \xi_y)/\partial(x, y, z, e_x, e_y, v)$ required for the tomographic matrix $\underline{\mathbf{F}}$ (12) can be calculated during ray tracing along the normal rays with ray perturbation theory (Farra and Madariaga, 1987). The relevant results of ray perturbation theory are summarized in this appendix.

The reduced ray-tracing system in 3D Cartesian coordinates can be obtained from the reduced Hamiltonian (e. g., Farra and Madariaga, 1987)

$$H = -\sqrt{v^{-2} - p_x^2 - p_y^2} = -p_z, \quad (\text{B1})$$

where p_x , p_y , and p_z are the components of the slowness vector, and the z -coordinate acts as the free parameter along the ray. The ray-tracing system reads

$$\begin{aligned} \frac{dx}{dz} &= \frac{\partial H}{\partial p_x} = \frac{p_x}{p_z} & \frac{dp_x}{dz} &= -\frac{\partial H}{\partial x} = -\frac{1}{v^3 p_z} \frac{\partial v}{\partial x} \\ \frac{dy}{dz} &= \frac{\partial H}{\partial p_y} = \frac{p_y}{p_z} & \frac{dp_y}{dz} &= -\frac{\partial H}{\partial y} = -\frac{1}{v^3 p_z} \frac{\partial v}{\partial y} \end{aligned} \quad (\text{B2})$$

If the notations $\boldsymbol{\eta} = (x, y, p_x, p_y)^T$ and $\Delta\boldsymbol{\eta} = (\Delta x, \Delta y, \Delta p_x, \Delta p_y)^T$ are introduced, the paraxial ray-tracing system can be written as

$$\frac{d}{dz} \Delta\boldsymbol{\eta} = \underline{\mathbf{S}} \Delta\boldsymbol{\eta} \quad (\text{B3})$$

where the matrix $\underline{\mathbf{S}}$ is given by

$$\underline{\mathbf{S}} = \begin{pmatrix} \frac{\partial^2 H}{\partial p_x \partial x} & \frac{\partial^2 H}{\partial p_x \partial y} & \frac{\partial^2 H}{\partial p_x \partial p_x} & \frac{\partial^2 H}{\partial p_x \partial p_y} \\ \frac{\partial^2 H}{\partial p_y \partial x} & \frac{\partial^2 H}{\partial p_y \partial y} & \frac{\partial^2 H}{\partial p_y \partial p_x} & \frac{\partial^2 H}{\partial p_y \partial p_y} \\ -\frac{\partial^2 H}{\partial x \partial x} & -\frac{\partial^2 H}{\partial x \partial y} & -\frac{\partial^2 H}{\partial x \partial p_x} & -\frac{\partial^2 H}{\partial x \partial p_y} \\ -\frac{\partial^2 H}{\partial y \partial x} & -\frac{\partial^2 H}{\partial y \partial y} & -\frac{\partial^2 H}{\partial y \partial p_x} & -\frac{\partial^2 H}{\partial y \partial p_y} \end{pmatrix}. \quad (\text{B4})$$

The associated propagator matrix will be denoted by $\underline{\mathbf{T}}$, equation (10). Thus, for the ray starting location z_0 and the ray end location z_1 ,

$$\Delta\boldsymbol{\eta}(z_1) = \underline{\mathbf{T}}(z_1, z_0) \Delta\boldsymbol{\eta}(z_0). \quad (\text{B5})$$

A perturbation Δv of the velocity model results in a perturbed Hamiltonian:

$$H = H_0 + \Delta H \quad \text{with} \quad \Delta H = \frac{\partial H}{\partial v} \Delta v. \quad (\text{B6})$$

It has been shown by Farra and Madariaga (1987) that this leads to a perturbation of the components of $\boldsymbol{\eta}$ given by

$$\Delta\boldsymbol{\eta} = \underline{\mathbf{T}}(z_1, z_0) \int_{z_0}^{z_1} \underline{\mathbf{T}}^{-1}(z', z_0) \Delta\mathbf{b}(z') dz' \quad (\text{B7})$$

with

$$\Delta\mathbf{b} = (\partial\Delta H/\partial p_x, \partial\Delta H/\partial p_y, -\partial\Delta H/\partial x, -\partial\Delta H/\partial y)^T. \quad (\text{B8})$$

The first-order effect of perturbations of the values of $\boldsymbol{\eta}$ and of perturbations of the velocity on the ray propagator matrix $\underline{\mathbf{T}}$ itself can be written as

$$\Delta\underline{\mathbf{T}} = \underline{\mathbf{T}}(z_1, z_0) \int_{z_0}^{z_1} \underline{\mathbf{T}}^{-1}(z', z_0) \Delta\underline{\mathbf{S}} \underline{\mathbf{T}}(z', z_0) dz', \quad (\text{B9})$$

where $\Delta\underline{\mathbf{S}} = \Delta\underline{\mathbf{S}}_1(\Delta v) + \Delta\underline{\mathbf{S}}(\Delta\boldsymbol{\eta})$ with

$$\Delta\underline{\mathbf{S}}_1 = \begin{pmatrix} \frac{\partial^2 \Delta H}{\partial p_x \partial x} & \frac{\partial^2 \Delta H}{\partial p_x \partial y} & \frac{\partial^2 \Delta H}{\partial p_x \partial p_x} & \frac{\partial^2 \Delta H}{\partial p_x \partial p_y} \\ \frac{\partial^2 \Delta H}{\partial p_y \partial x} & \frac{\partial^2 \Delta H}{\partial p_y \partial y} & \frac{\partial^2 \Delta H}{\partial p_y \partial p_x} & \frac{\partial^2 \Delta H}{\partial p_y \partial p_y} \\ -\frac{\partial^2 \Delta H}{\partial x \partial x} & -\frac{\partial^2 \Delta H}{\partial x \partial y} & -\frac{\partial^2 \Delta H}{\partial x \partial p_x} & -\frac{\partial^2 \Delta H}{\partial x \partial p_y} \\ -\frac{\partial^2 \Delta H}{\partial y \partial x} & -\frac{\partial^2 \Delta H}{\partial y \partial y} & -\frac{\partial^2 \Delta H}{\partial y \partial p_x} & -\frac{\partial^2 \Delta H}{\partial y \partial p_y} \end{pmatrix} \quad (\text{B10})$$

and

$$\Delta \underline{\mathbf{S}}_2 = \left[\Delta x \frac{\partial}{\partial x} + \Delta y \frac{\partial}{\partial y} + \Delta p_x \frac{\partial}{\partial p_x} + \Delta p_y \frac{\partial}{\partial p_y} \right] \begin{pmatrix} \frac{\partial^2 H_0}{\partial p_x \partial x} & \frac{\partial^2 H_0}{\partial p_x \partial y} & \frac{\partial^2 H_0}{\partial p_x \partial p_x} & \frac{\partial^2 H_0}{\partial p_x \partial p_y} \\ \frac{\partial^2 H_0}{\partial p_y \partial x} & \frac{\partial^2 H_0}{\partial p_y \partial y} & \frac{\partial^2 H_0}{\partial p_y \partial p_x} & \frac{\partial^2 H_0}{\partial p_y \partial p_y} \\ -\frac{\partial^2 H_0}{\partial x \partial x} & -\frac{\partial^2 H_0}{\partial x \partial y} & -\frac{\partial^2 H_0}{\partial x \partial p_x} & -\frac{\partial^2 H_0}{\partial x \partial p_y} \\ -\frac{\partial^2 H_0}{\partial y \partial x} & -\frac{\partial^2 H_0}{\partial y \partial y} & -\frac{\partial^2 H_0}{\partial y \partial p_x} & -\frac{\partial^2 H_0}{\partial y \partial p_y} \end{pmatrix}. \quad (\text{B11})$$

All partial derivatives are evaluated on the central ray. The perturbations Δx , Δy , Δp_x , and Δp_y in equation (B11) are obtained from equation (B5). An additional relation linearly relates perturbations of the propagator matrix to changes of the ray starting location along the z-axis:

$$\Delta \underline{\mathbf{T}} = -\underline{\mathbf{T}}(z_1, z_0) \underline{\mathbf{S}}|_{z=z_0} \Delta z_0. \quad (\text{B12})$$

Together with the expression

$$\Delta \underline{\mathbf{M}}_h = (\Delta \underline{\mathbf{D}} - \underline{\mathbf{D}} \underline{\mathbf{B}}^{-1} \Delta \underline{\mathbf{B}}) \underline{\mathbf{B}}^{-1}, \quad (\text{B13})$$

equations (B9) - (B12) can be used to calculate the Fréchet derivatives involving $\underline{\mathbf{M}}_h$. The corresponding component in a given azimuth direction ϕ is then directly calculated with an equation of the form of (5).

The Fréchet derivatives involving the data components p_{ξ_x} , p_{ξ_y} , ξ_x , and ξ_y can be obtained from equations (B5) - (B7) and the additional relations

$$\begin{pmatrix} \Delta x_1 \\ \Delta y_1 \end{pmatrix} = -\underline{\mathbf{A}} \begin{pmatrix} p_{x_0} \\ p_{y_0} \end{pmatrix} \frac{\Delta z_0}{p_{z_0}}, \quad \begin{pmatrix} \Delta p_{x_1} \\ \Delta p_{y_1} \end{pmatrix} = -\underline{\mathbf{C}} \begin{pmatrix} p_{x_0} \\ p_{y_0} \end{pmatrix} \frac{\Delta z_0}{p_{z_0}}. \quad (\text{B14})$$

Here, an index 0 denotes properties at the ray starting location, while an index 1 denotes properties at the ray end location. Finally, the Fréchet derivatives involving the traveltimes τ along the normal ray follow from

$$\Delta \tau = -p_{x_0} \Delta x_0 - p_{y_0} \Delta y_0 - p_{z_0} \Delta z_0 - \int_{z_0}^{z_1} \frac{\Delta v}{v^3 p_z} dz. \quad (\text{B15})$$